



Optical parametric amplification by monolayer transition metal dichalcogenides

Chiara Trovatello^{1,2}, Andrea Marini³, Xinyi Xu¹, Changhwan Lee¹, Fang Liu⁴, Nicola Curreli ^{1,5}, Cristian Manzoni ⁶, Stefano Dal Conte ², Kaiyuan Yao¹, Alessandro Ciattoni⁷, James Hone ¹, Xiaoyang Zhu ⁴, P. James Schuck ¹ and Giulio Cerullo ^{2,6}

Optical parametric amplification is a second-order nonlinear process whereby an optical signal is amplified by a pump via the generation of an idler field. This mechanism is inherently related to spontaneous parametric down-conversion, which currently constitutes the building block for entangled photon pair generation², a process that is exploited in modern quantum technologies. Here we demonstrate single-pass optical parametric amplification at the ultimate thickness limit; using semiconducting transition metal dichalcogenides^{3,4}, we show that amplification can be attained over propagation through a single atomic layer. Such a second-order nonlinear interaction at the two-dimensional limit bypasses phase-matching requirements⁵ and achieves ultrabroad amplification bandwidths. In agreement with first-principle calculations, we observe that the amplification process is independent of the in-plane polarization of signal and pump fields. By the use of AA-stacked multilayers, we present a clear pathway towards the scaling of conversion efficiency. Our results pave the way for the development of atom-sized tunable sources of radiation with potential applications in nanophotonics and quantum information technology.

When an intense electromagnetic wave interacts with matter, the induced polarization drives a plethora of nonlinear physical phenomena such as frequency conversion⁶, all-optical self-effects⁷ and generation of non-classical radiation². In particular, spontaneous parametric down-conversion (SPDC) is a second-order nonlinear process where a pump photon $(\hbar\omega_p)$ annihilates into a signal $(\hbar\omega_s)$ and an idler photon $(\hbar\omega_i)$ according to energy conservation $\hbar\omega_{\rm p} = \hbar\omega_{\rm s} + \hbar\omega_{\rm i}$. SPDC underpins optical parametric amplification (OPA) and oscillation (OPO), which are exploited in tunable sources of coherent radiation^{8,9} and for the generation of entangled photons and squeezed states of light10. Current OPA/OPO set-ups exploit millimetre-thick anisotropic crystals with broken inversion symmetry that enable momentum conservation by birefringence phase matching^{11,12}, thus limiting amplification bandwidths. Here we show that single-layer transition metal dichalcogenides (1L-TMDs)—due to the two-dimensional nonlinear interaction, which does not introduce any dispersion-induced phase mismatch—enable single-pass collinear OPA at the atomic scale without the phase-matching constraint. The OPA process is insensitive to the TMD crystal orientation and to the pump and signal polarizations. As expected for a two-dimensional material, the idler intensity scales linearly with pump and signal powers. Our experimental findings are fully

supported by first-principle theoretical calculations based on the tight-binding model and Bloch independent electron dynamics⁵, indicating that the observed phenomena are a direct consequence of the D_{3h} symmetry group of such crystals.

Transition metal dichalcogenides are layered semiconducting materials that can be reduced to single-layer thicknesses due to the weak van der Waals interlayer forces. Single-layer transition metal dichalcogenides are two-dimensional semiconductors, which, despite vanishing (<1 nm) thicknesses, exhibit very strong lightmatter interactions due to quantum confinement effects^{3,4}. This class of materials also possesses second-order susceptibilities ($\chi^{(2)}$) that are orders of magnitude higher than in conventional nonlinear materials^{13–20}. We demonstrate the OPA process over multiple group-six 1L-TMDs, namely, MoSe₂, MoS₂, WSe₂ and WS₂.

The monolayers are prepared using a gold-assisted exfoliation technique (see Methods), which enables the fabrication of large-area (millimetre-size) samples²¹. The monolayers are subsequently transferred onto 500-μm-thick SiO₂ substrates. Samples are illuminated by a ×40 reflective objective with two collinear and synchronized femtosecond laser beams—pump and signal—that are supplied by a Ti:sapphire oscillator and an OPO, respectively, both of which operate at 80 MHz. The pump at 3.11 eV is obtained by frequency doubling the output of the oscillator. The OPO signal is tunable from 0.83 eV to 1.21 eV. Pump and signal beams are overlapped in space and synchronized in time at the sample plane. The nonlinear emission is collected in a backscattering geometry onto a silicon electron multiplication charge-coupled device (EMCCD) camera (see Methods)

In an OPA process, the pump photons are annihilated into pairs of signal and idler photons, following the energy conservation constraint (Fig. 1a, top and bottom). We measure the idler beam—which is the difference frequency between pump and signal—as a fingerprint of the OPA process due its background free detection.

Figure 1 demonstrates the broadband tunability and quantifies the efficiency of the OPA process in 1L-TMDs²². Figure 1a shows the normalized idler spectra measured on a monolayer of MoSe₂ in a broad photon energy range from 1.90 eV to 2.28 eV. The finite spectral window is solely limited by the tunability of our signal beam. Figure 1b shows four panels that report the absolute values of the effective generated idler power (coloured dots) measured across the four semiconducting 1L-TMDs, having already accounted for all of the estimated experimental losses (see Methods). For each TMD, the efficiency curves are measured on a single spot of the sample.

¹Department of Mechanical Engineering, Columbia University, New York, NY, USA. ²Dipartimento di Fisica, Politecnico di Milano, Milano, Italy. ³Department of Physical and Chemical Sciences, University of L'Aquila, L'Aquila, Italy. ⁴Department of Chemistry, Columbia University, New York, NY, USA. ⁵Graphene Labs, Istituto Italiano di Tecnologia, Genova, Italy. ⁶IFN-CNR, Milano, Italy. ⁷Dipartimento di Scienze Fisiche e Chimiche, CNR-SPIN, L'Aquila, Italy. [∞]e-mail: p.j.schuck@columbia.edu; giulio.cerullo@polimi.it

NATURE PHOTONICS LETTERS

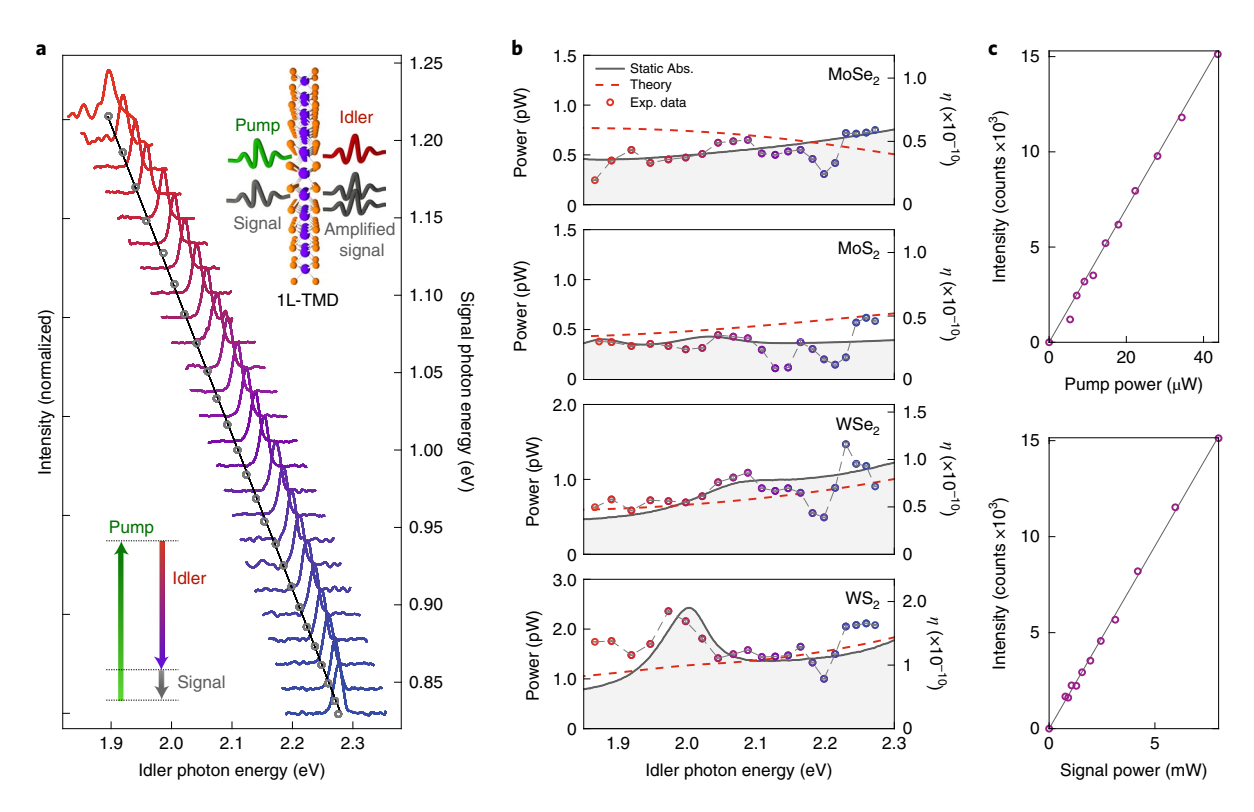


Fig. 1 | Broadband OPA in 1L-TMDs. a, Normalized tunable idler spectra measured on 1L-MoSe₂; the spectra are vertically offset. The nominal idler photon energy (black solid line) and measured peak values (grey dots) are shown. **b**, Absolute idler power and efficiency (η) as a function of the idler photon energy measured on the four semiconducting 1L-TMDs (coloured dots), as well as the corresponding calculated theoretical efficiencies divided by a factor of 2.5 (dashed lines). The pump polarization is linear and vertical, whereas the signal polarization is linear and horizontal. Pump and signal beams are focused down to spot sizes of ~1 μm and ~2 μm, and have fluences of ~77 μJ cm⁻² (~48.3 μW) and ~5 mJ cm⁻² (~12.7 mW), respectively; for each idler photon energy, the error bars—calculated at each data point as the standard deviation of five different spectra acquired with an integration time of 1 s—are between two and three orders of magnitude smaller than the absolute idler power, that is, laser power fluctuations are averaged out over 1s integration time (see Supplementary Note 4). Absorption spectra (grey areas), measured on each individual TMD, are multiplied by a scaling factor and overlapped onto the efficiency curves. **c**. The idler linear intensity dependence on pump and signal powers measured on 1L-MoSe₂.

Spatial inhomogeneities of the TMDs introduce fluctuations in the nonlinear signal on the order of ~5% (see Supplementary Note 5). The ~500 μm SiO $_2$ substrate does not provide any appreciable nonlinear signal in the observed spectral window under the same experimental conditions (see Supplementary Fig. 12).

Although excitons have been shown to play a relevant role in the linear and nonlinear optical properties of 1L-TMDs^{23,24}, the almost frequency-independent efficiency of idler generation observed for all of the 1L-TMDs (see Fig. 1b) implies that they play a minor role in the OPA process for the considered photon energies and intensities of pump and signal fields. Although experimental data of linear absorption in Fig. 1b indicate the occurrence of exciton resonances for WS₂ (A-exciton), WSe₂ (B-exciton) and MoS₂ (both A and B excitons) in the considered idler photon energy range, the idler nonlinear signal is weakly affected by such resonances due to their low quality factors. In particular, in spite of A and B exciton resonances (see Supplementary Note 1), there is not any enhancement in the nonlinear signal generation for MoS2, whereas there is weak enhancement (at most by a factor of two) for WS₂. This result contrasts the resonant behaviour of the second-harmonic generation (SHG) process observed around the excitons^{25,26}.

Our theoretical predictions (red dashed lines in Fig. 1b) are based on independent electron dynamics that are accounted by a $\mathbf{k}\cdot\mathbf{p}$ time-dependent Hamiltonian $H_0(t)$ leading to the density matrix temporal evolution $\dot{\rho}=-(i/\hbar)[H_0(t),\rho]-(1/\tau)(\rho-\rho_0)$, where \mathbf{k} is the electron wave-vector, \mathbf{p} is the optical momentum, ρ is the density matrix and a phenomenological relaxation is assumed to bring

the system to the relaxed state ρ_0 at a rate τ^{-1} with $\hbar\tau^{-1}=50\,\mathrm{meV}$ (see Methods and Supplementary Note 8). Such density matrix equations are solved perturbatively, thus enabling the calculation of the nonlinear polarization and the nonlinear mixing susceptibilities $\chi^{(2)}(\omega_p,\omega_{s,i})$. Our calculations attribute the flat and almost featureless idler generation efficiency to off-resonant interband dynamics, whereas the observed ultrabroad bandwidth of the OPA process is related to the vanishing thickness of the nonlinear material, which eliminates any phase mismatch⁵.

The spectral efficiency profile can be estimated by seeding the OPA with either an ultrabroadband light pulse or a tunable monochromatic seed pulse. We adopted the latter approach, seeding the OPA with a tunable narrowband signal, and measuring the spectrum and energy of the idler as a function of the signal centre frequency. The resulting intensity thus samples the OPA gain spectrum and proves the ultrabroad bandwidth amplification in 1L-TMDs, which is a direct consequence of the absence of phase-matching constraints (see Supplementary Note 7).

Owing to the D_{3h} group symmetry of 1L-TMDs, the second-order nonlinear susceptibility tensor is characterized by only one parameter, $\chi^{(2)}(\omega_p,\ \omega_s)^{1,13}$. Our theoretical calculations indicate that the broadband spectrum of the OPA process ensues from a non-resonant effective $|\chi^{(2)}(\omega_p,\ \omega_s)| \simeq 2-8\times 10^{-10}\,\mathrm{m\,V^{-1}}$ for the 1L-TMDs (see Methods and Supplementary Note 8), which is of the same order of magnitude of the resonant $|\chi^{(2)}|$ of typical bulk semiconductors such as GaAs, which cannot be easily reduced to a single layer²⁷. Figure 1c shows a linear dependence of the idler

LETTERS NATURE PHOTONICS

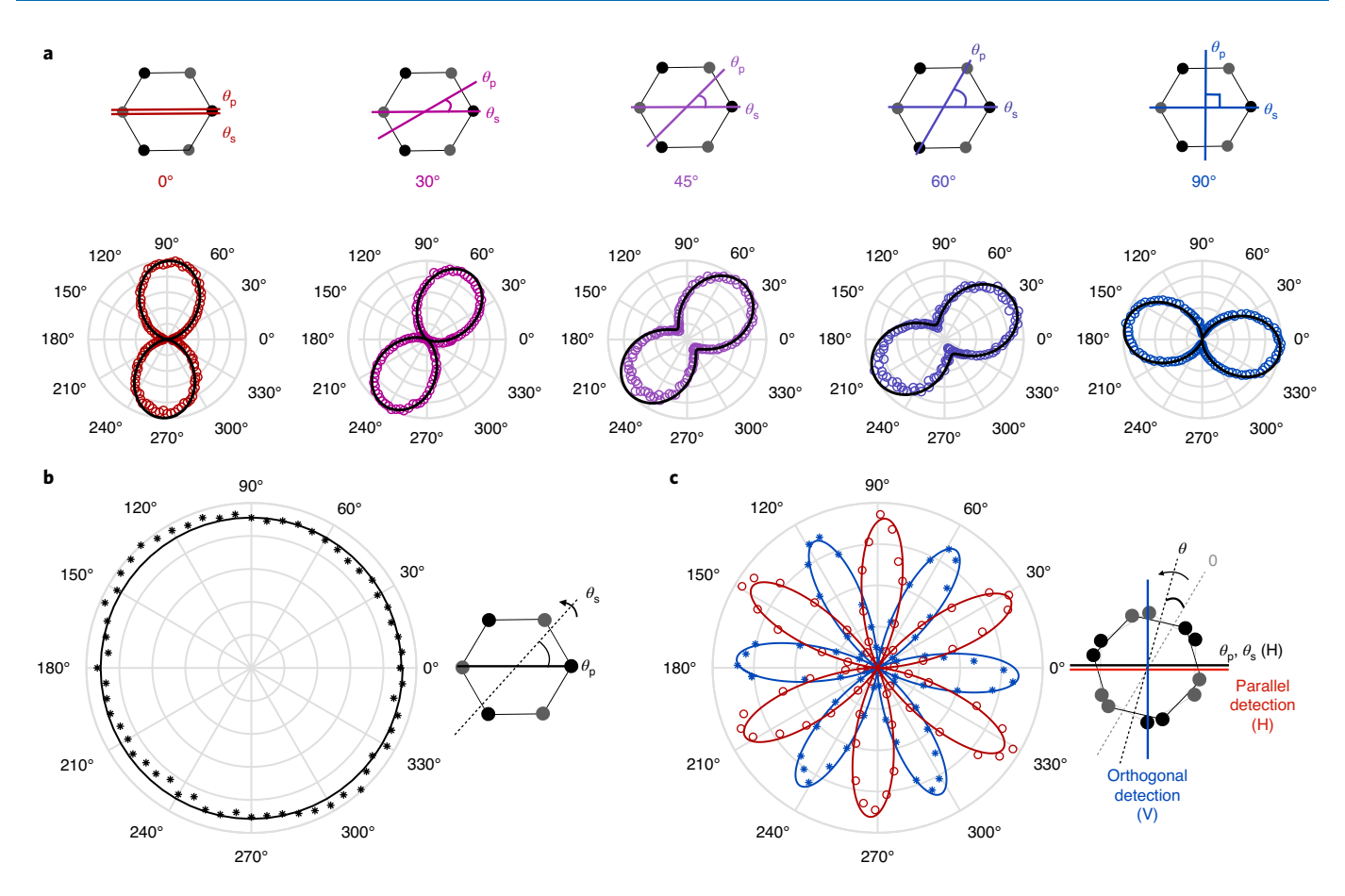


Fig. 2 | Idler polarization. **a**, Polar plots of the measured polarization emission of the idler beam at 2.15 eV (coloured dots) and fitting functions (black lines) $f \propto \cos^2(\theta + \phi)$. The signal polarization is linear and horizontal (0°) whereas the pump polarization is tuned at the discrete values 0°, 30°, 45°, 60°, 90°, as depicted in the input polarization schemes above the polar plots. **b**, A polar plot of the idler spectrum intensity (asterisks) centred at 2.15 eV as a function of $\theta_s - \theta_p$, as well as a fitting constant function (continuous line). **c**, A polar plot of the idler intensity as a function of the crystal's azimuthal angle θ (asterisks/circles). Red and blue colours indicate the parallel (H) and orthogonal (V) components of the idler intensity with respect to pump and signal beams, which are set to be linearly polarized to 0° (H). The fitting function (continuous line) for both detection configurations is $f \propto \cos^2(3\theta + \phi)$ relative to the armchair direction. All the data in panels **a-c** have been measured on 1L-WSe₂ as a representative of 1L-TMDs.

intensity with pump and signal power measured on 1L-MoSe₂, which is in agreement with the theory that accurately reproduces such dependence in the undepleted pump approximation and weak excitation regime (see Methods and Supplementary Notes 7 and 8). The other TMDs (WS₂, WSe₂ and MoS₂) show a similar behaviour (see Supplementary Fig. 6).

The theoretical analysis of the OPA process in such 1L-TMDs, in addition to providing the second-order nonlinear susceptibility tensor, reveals the polarization dependence of the amplified signal field and generated idler field. The D_{3h} group symmetry implies that the OPA efficiency does not depend on the absolute and the mutual polarizations of signal and pump fields (see Supplementary Note 8). Conversely, the polarization of the idler signal θ_i is fixed by the pump and signal in-plane polarization angles θ_p and θ_s , respectively, with respect to the armchair crystallographic axis and follows the rule $\theta_i = \pi/2 - \theta_p - \theta_s$, which we confirm experimentally.

Figure 2a reports polar plots of the idler generation efficiency for different pump polarization angles for 1L-WSe₂. The signal polarization is kept horizontal (θ_s =0°) while the pump polarization is rotated by a half-wave plate at five discrete angles: θ_p =0°, 30°, 45°, 60°, 90°. The polar measurements depicted in Fig. 2a are taken by rotating an analyser in front of the detector. The coloured circles represent the measured experimental data, whereas the black lines are the fitting curves obtained using the function $\cos^2(\theta + \phi)$, where

 θ and ϕ represent the polarizer angle and an offset angle, respectively, confirming the theoretical prediction of a linearly polarized idler signal and the dependence of θ_i over θ_s and θ_p .

Figure 2b shows the normalized total emitted idler intensity at 2.15 eV as a function of the signal–pump polarization angle $(\theta_s - \theta_p)$ measured on 1L-WSe₂. The pump polarization is linear and horizontal (0°) while the signal polarization is rotated from 0° to 360°. The data display an efficiency independent of the relative angle between pump and signal polarization directions, which is in agreement with theoretical predictions.

The dependence of the idler intensity on the crystallographic orientation is reported in Fig. 2c for the parallel and orthogonal directions of the polarizer axis in detection. These polar plots reproduce results previously reported with SHG, confirming the sixfold symmetric second-order nonlinear tensor of the material¹³. As the other TMDs (WS₂, MoS₂ and MoSe₂) belong to the same D_{3h} symmetry group, they display qualitative behaviour identical to those in Fig. 2 under the same experimental conditions, as shown in Supplementary Fig. 7 for the emitted idler polarization with 0°-0° and 0°-90° signal-pump input polarization configurations, for the efficiency dependence on θ_s - θ_p , and in Supplementary Fig. 3 for SHG polar measurements.

In our operating regime, the gain of the second-order parametric process scales quadratically with the thickness of the nonlinear

NATURE PHOTONICS LETTERS

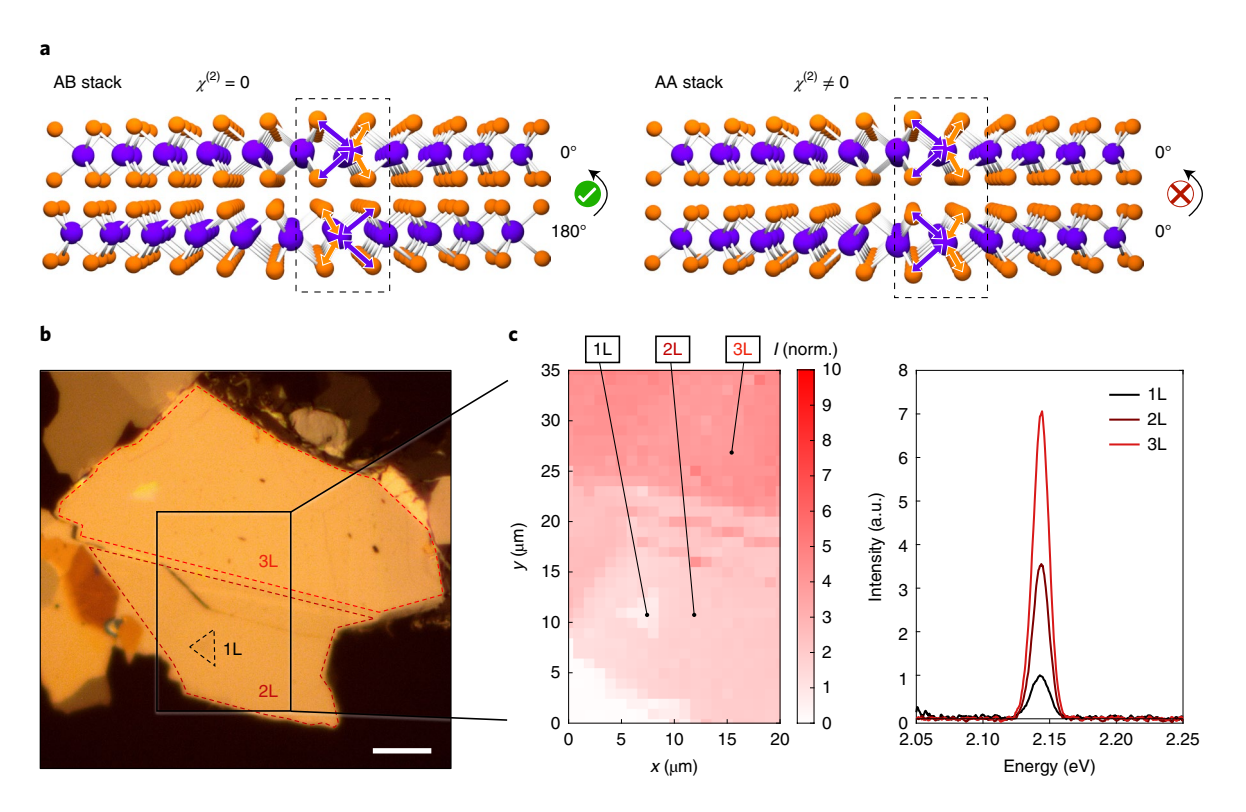


Fig. 3 | Efficiency scaling with AA stacking. a, Schematics of AB and AA stacking orders. Left: a natural centrosymmetric AB structure with an interlayer twist angle of 180° ($\chi^{(2)}$ = 0). Right: an artificial non-centrosymmetric AA configuration with a twist angle of 0° ($\chi^{(2)}$ \neq 0). **b**, A micrograph of the WS₂ AA stack sample; the dashed areas mark 1L, 2L and 3L regions. Scale bar, 10 μm. **c**, A normalized idler emission intensity map (I) over a sample area with 1L, 2L and 3L portions (left), and the extracted idler spectra as a function of the number of layers (right). Pump and signal beams have linear and horizontal polarization and their fluence is set to ~100 μJ cm⁻² and ~2 mJ cm⁻², respectively.

medium. The effective OPA gain could, in principle, therefore be boosted by increasing the number of TMD layers in the sample. Unfortunately, in the natural vertical stacking of the most commonly used semiconducting multilayer TMDs (2H polytype), each constituent layer is rotated by 180° with respect to its next neighbours, forming so-called AB stacks²⁹ (depicted in Fig. 3a, left). As a direct consequence, the inversion symmetry in TMD samples with an even number of layers is restored ($|\chi^{(2)}|=0$), suppressing the enhancement of second-order nonlinear processes with thickness. One strategy to increase the OPA effective gain is to vertically stack several monolayers with interlayer ~0° crystal angle alignment, preserving the broken inversion symmetry $(|\chi^{(2)}| \neq 0)$ and forming the so-called AA stack²⁸ (Fig. 3a, right). Due to the atomic thickness of TMDs, many layers can be stacked on top of each other while still maintaining a deeply subwavelength thickness, avoiding phase-matching constraints. In an ideal lossless case, the OPA efficiency is expected to scale as the square of the number of layers N(refs. 21,29).

We have performed a proof-of-principle demonstration of this concept for 1–3 layers of manually AA-stacked WS₂, as shown in Fig. 3b. We can distinguish 1L, 2L and 3L-WS₂ regions, sitting on top of a ~30 nm hexagonal boron nitride (hBN) flake (see Supplementary Note 2). The whole AA stack is transferred on top of a 500- μ m-thick SiO₂ substrate. The 1L, 2L and 3L regions have been identified by photoluminescence characterization (see Supplementary Fig. 4). Figure 3b shows the emitted idler spectrum at 2.14 eV as a function of the number of WS₂ layers. Pump and signal photon energies are set to 3.11 eV and 0.97 eV, respectively, and both beams have parallel and horizontal polarizations with respect to the sample plane. The underlying hBN flake does not give an appreciable second-order nonlinear signal within our experimental conditions, as $|\chi^{(2)}|$ for

bulk hBN is two to three orders of magnitude smaller than for 1L-TMDs¹³. The measured idler intensity indeed scales nearly quadratically with the layer number. The observed deviation from the N^2 trend is due to the absorption of the 3.11 eV pump beam, which lies above the bandgap of WS₂ ($\alpha_{\rm p} \approx 7\%$) and to the partial reabsorption of the emitted idler field ($\alpha_{\rm i} \approx 3\%$; see Supplementary Note 6). Such absorption effects can be avoided by tuning the pump photon energy below the bandgap of the TMD; AA stacking thus offers a clear route for scaling the efficiency of the OPA process in TMDs in view of their applications in photonic devices. Similarly, non-centrosymmetric 3R-oriented TMD crystals can be used, which are directly grown via chemical vapour deposition²⁹.

In conclusion, our experimental and theoretical investigations provide the first evidence of OPA at the ultimate thickness limit by a single pass through 1L-TMDs. We find that the amplification efficiencies of MoS₂, MoSe₂, WS₂ and WSe₂ are comparable and that their frequency dependence is relatively flat, thus enabling broadband functionality. The measured efficiencies and polarization of the nonlinear process are reproduced by first-principle calculations based on Bloch independent electron dynamics. The OPA process in 1L-TMDs is observed across an ultrabroad spectral range, bypassing phase matching constraints: this is generally unattainable in standard photonic materials owing to destructive interference produced by chromatic dispersion. Artificial stacking of AA aligned TMD monolayers provides a route for quadratic scaling of the efficiency with layer number, while still maintaining the ultrabroad bandwidth enabled by the deeply subwavelength regime. Moreover, the relative ease of combining TMD layers with other micro- and nanophotonic technologies—including distributed Bragg reflectors and low-loss metasurfaces—offers an immediate pathway for further boosting efficiencies by several orders of magnitude.

LETTERS NATURE PHOTONICS

The implementation of broadband, highly efficient nonlinear frequency conversion in structures with ultracompact footprints is essential for new photonic technologies required to address rising demands for fast, energy-efficient information processing. The large $\chi^{(2)}$ of 1L-TMDs (one to two orders of magnitude higher than in current crystals used for OPA and SPDC processes) paves the way to the scaling and the integration of two-dimensional materials in photonic applications, such as two-dimensional all-optical amplifiers, on-chip frequency converters and integrated nanoscale sources of entangled photons for quantum information science.

Online content

Any methods, additional references, Nature Research reporting summaries, source data, extended data, supplementary information, acknowledgements, peer review information; details of author contributions and competing interests; and statements of data and code availability are available at https://doi.org/10.1038/s41566-020-00728-0.

Received: 17 February 2020; Accepted: 26 October 2020; Published online: 21 December 2020

References

- 1. Shen, Y. R. The Principles of Nonlinear Optics (John Wiley & Sons, 1984).
- 2. Kwiat, P. G. et al. New high-intensity source of polarisation-entangled photon pairs. *Phys. Rev. Lett.* **75**, 4337–4341 (1995).
- Chernikov, A. et al. Exciton binding energy and nonhydrogenic rydberg series in monolayer WS₂. Phys. Rev. Lett. 113, 076802 (2014).
- Qiu, D. Y., da Jornada, F. H. & Louie, S. G. Optical spectrum of MoS₂: many-body effects and diversity of exciton states. *Phys. Rev. Lett.* 111, 216805 (2013).
- Ciattoni, A., Marini, A., Rizza, C. & Conti, C. Phase-matching-free parametric oscillators based on two-dimensional semiconductors. *Light Sci. Appl.* 7, 5 (2018).
- Franken, P. A., Hill, A. E., Peters, C. W. & Weinreichet, G. Generation of optical harmonics. *Phys. Rev. Lett.* 7, 118–119 (1961).
- Stegeman, G. I., Hagan, D. J. & Torner, L. χ⁽²⁾ Cascading phenomena and their applications to all-optical signal processing, mode-locking, pulse compression and solitons. *Opt. Quant. Electron.* 28, 1691–1740 (1996).
- Giordmaine, J. A. & Miller, R. C. Tunable coherent parametric oscillation in LiNbO₃ at optical frequencies. *Phys. Rev. Lett.* 14, 973–976 (1965).
- Yariv, A. & Louisell, W. H. Theory of the optical parametric oscillator. IEEE J. Quant. Electron. 9, 418–424 (1966).
- Wu, L.-A., Xiao, M. & Kimble, H. J. Squeezed states of light from an optical parametric oscillator. J. Opt. Soc. Am. B 4, 1465–1475 (1987).

- Giordmaine, J. A. Mixing of light beams in crystals. Phys. Rev. Lett. 8, 19–20 (1962).
- Canalias, C. & Pasiskevicius, V. Mirrorless optical parametric oscillator. Nat. Photon. 1, 459–462 (2007).
- 13. Li, Y. et al. Probing symmetry properties of few-layer MoS₂ and h-BN by optical second-harmonic generation. *Nano Lett.* **13**, 3329–3333 (2013).
- Yin, X. Edge nonlinear optics on a MoS₂ atomic monolayer. Science 344, 488–490 (2014).
- Majumdar, A. et al. Hybrid 2D material nanophotonics: a scalable platform for low-power nonlinear and quantum optics. ACS Photon. 2, 1160–1166 (2015).
- Woodward, R. I. et al. Characterization of the second- and third-order nonlinear optical susceptibilities of monolayer MoS₂ using multiphoton microscopy. 2D Mater. 4, 011006 (2016).
- Yu, S., Wu, X., Wang, Y., Guo, X. & Tong, L. 2D materials for optical modulation: challenges and opportunities. Adv. Mater. 29, 1606128 (2017).
- Säynätjoki, A. et al. Ultra-strong nonlinear optical processes and trigonal warping in MoS₂ layers. Nat. Commun. 8, 893 (2017).
- Autere, A. et al. Optical harmonic generation in monolayer group-VI transition metal dichalcogenides. *Phys. Rev. B* 98, 115426 (2018).
- Mennel, L., Paur, M. & Mueller, T. Second harmonic generation in strained transition metal dichalcogenide monolayers: MoS₂, MoSe₂, WS₂, and WSe₂. APL Photon. 4, 034404 (2019).
- Liu, F. et al. Disassembling 2D van der Waals crystals into macroscopic monolayers and reassembling into artificial lattices. *Science* 367, 903–906 (2020).
- Trovatello C. et al. Broadband optical parametric amplification by two-dimensional semiconductors. Preprint at https://arxiv.org/abs/1912.10466 (2019).
- Ugeda, M. M. et al. Giant bandgap renormalization and excitonic effects in a monolayer transition metal dichalcogenide semiconductor. *Nat. Mater.* 13, 1091–1095 (2014).
- Selig, M. et al. Excitonic linewidth and coherence lifetime in monolayer transition metal dichalcogenides. Nat. Commun. 7, 13279 (2016).
- Wang, G. et al. Giant enhancement of the optical second-harmonic emission of WSe₂ monolayers by laser excitation at exciton resonances. *Phys. Rev. Lett.* 114, 097403 (2015).
- Seyler, K. L. et al. Electrical control of second-harmonic generation in a WSe₂ monolayer transistor. Nat. Nanotechnol. 10, 407–411 (2015).
- 27. Bergfeld, S. & Daum, W. Second-harmonic generation in gaas: experiment versus theoretical predictions of $\chi_{xyz}^{(2)}$. *Phys. Rev. Lett.* **90**, 036801 (2003).
- He, J., Hummer, K. & Franchini, C. Stacking effects on the electronic and optical properties of bilayer transition metal dichalcogenides MoS₂, MoSe₂, WS₂, and WSe₂. Phys. Rev. B 89, 075409 (2014).
- Zhao, M. et al. Atomically phase-matched second-harmonic generation in a 2D crystal. Light Sci. Appl. 8, e16131 (2016).

Publisher's note Springer Nature remains neutral with regard to jurisdictional claims in published maps and institutional affiliations.

© The Author(s), under exclusive licence to Springer Nature Limited 2020

NATURE PHOTONICS LETTERS

Methods

Sample preparation. The monolayers MoS_2 , WS_2 , $MoSe_2$, WSe_2 on SiO_2 substrate are prepared from bulk WS_2 , $MoSe_2$, WSe_2 (HQ Graphene) and MoS_2 (SPI Supplies) single crystals using a gold-assisted exfoliation technique published previously 30 . Briefly, a layer of gold is prepared on top of the bulk crystals. The gold layer is exfoliated away with a thermal release tape (Semiconductor Corporation), carrying a large piece of TMD monolayer on the contact surface, and is transferred onto a SiO_2 substrate. The thermal release tape is removed by heating to $130\,^{\circ}$ C. The tape residues are cleaned by acetone and O_2 plasma treatment. The gold layer is dissolved with a gold etchant solution, which is made from mixing KI (99.9%, Alfa Aesar) and I_2 (99.99%, Alfa Aesar) in deionized water. The exfoliated monolayers have a clean surface and strong photoluminescence that is comparable with the monolayers from conventional scotch tape exfoliation 30 .

The AA-stacked WS2 sample is prepared by employing a dry, contamination-free transfer procedure in which flakes are assembled into a perfectly oriented heterostructure (~0° crystal angle mismatch). A ~30-nm-thick hBN crystal (see atomic force microscopy profile in the Supplementary Fig. 5) is used as a sacrificial layer to allow the pick-up of 1L-WS2 crystals. Hexagonal boron nitride and 1L-WS₂ crystals are separately exfoliated on SiO₂ substrates through mechanical and gold-assisted large-area exfoliation, respectively30. A polypropylene carbonate polymer on a polydimethylsiloxane elastomer stamp is used to peel a hBN flake directly off the substrate under an optical microscope. To do this, the stamp is attached to a three-axis (XYZ) manipulator with the flakes facing towards the sample. With the same procedure, the hBN flake is positioned over the 1L-WS, flake; as the stamp is transparent, one can see the sample through it, it is therefore possible to align the edges of hBN and WS2. The two flakes are then brought into contact while the whole system is heated to promote adhesion between the flakes. The two flakes develop a strong van der Waals adhesion and, as a result, the 1L-WS₂ is torn and peeled off its substrate as the elastomer stamp is raised. A second 1L-WS2 flake is vertically added to the stack following the same procedure. To guarantee ~0° crystal angle mismatch among all of the stacked layers, the hBN/1L-WS₂ stack is exclusively translated on top of the remaining large-area 1L-WS2. The third 1L-WS2 flake is finally peeled off its substrate from hBN/1L-WS₂/1L-WS₂. Once the stacking procedure is completed, the pristine 500-μm-thick SiO₂ wafer acceptor substrate is positioned onto the sample's XYZ manipulator and the stack is deposited on it for further characterization. The experimental set-up employed to transfer the two-dimensional crystals consists of a custom built Signatone CM300 transfer station.

Experimental set-up. The laser source is a Ti:sapphire oscillator (Coherent Chameleon Ultra II), which emits 150 fs pulses at 1.55 eV, with a repetition rate of 80 MHz and an average output power of 4 W. The oscillator pumps an OPO, emitting a tunable signal from 0.83 eV to 1.21 eV. The pump beam at 3.11 eV is obtained by frequency doubling the laser output via a type I 2-mm-thick beta barium borate crystal. The 1.55 eV laser is focused on the beta barium borate crystal with a lens of focal distance f = 50 mm, and the generated second harmonic at 3.11 eV is collimated with a f = 75 mm lens. As the 1.55 eV beam has a linear horizontal polarization, the generated 3.11 eV beam has a linear vertical polarization. The fundamental beam is filtered out by a short-pass 500 nm (2.48 eV) filter, which is placed after the nonlinear crystal. The pump polarization is rotated by a half-wave plate. Pump and signal beams are temporally synchronized by a mechanically controlled translation stage. The two beams are combined on a beam-splitter (50:50 non-polarizing plate, Thorlabs BSW11R) and then coupled to a $\times 40$ reflective objective with a numerical aperture = 0.5 via a second non-polarizing plate BSW11R. The spatial overlap at the sample plane is achieved by imaging the sample and the laser spots on a silicon camera. The choice of a reflective objective is motivated by the achromatic focusing. The estimated diametres of pump and signal beams on the sample are $\sim 1 \, \mu m$ and ~2 µm, respectively. In all of the reported experiments the pump fluence range is $10-150\,\mu J\,cm^{-2}$ and the signal fluence range is $250\,\mu J\,cm^{-2}$ to $5\,mJ\,cm^{-2}.$ The lower fluence of the pump is motivated by the above-bandgap excitation. Both pump and signal intensities are adjusted by variable neutral density attenuators. At the sample plane, if we account for the dispersion introduced by the crossed transmissive optics, the pump and signal pulse duration is ~250 fs. The detection process occurs in a backscattering geometry. The measured total collection efficiency of the objective is 27.4% and it is constant across the spectral bandwidth of our experiment. In the extracted absolute efficiency for the OPA process, we also consider that the collected idler power is actually half of the total emitted power. Due to the fact that the idler is generated in the nonlinear process, the reflected and transmitted idler powers coincide owing to the continuity of the electric field at the 1L-TMD plane, that is, $\mathbf{E}_R^{(i)} = \mathbf{E}_\Gamma^{(i)}$ (no incident field oscillates at the idler frequency, $\mathbf{E}_0^{(i)} = 0$). In the accounted losses of our system, we also include the 50:50 non-polarizing beam-splitter (Thorlabs BSW11R) transmission, for each idler photon energy and polarization, and the reflectivity of the two silver mirrors before the silicon EMCCD camera. The polarization- and grating-dependent count/photon ratio of the silicon EMCCD camera is carefully measured across a broad spectral range, fully covering our experimental working region, to directly convert the number of counts into number of photons, that is, power. After the interaction with the sample, in the collection path the input laser beams are

filtered out by two 500 nm (2.48 eV) short-pass and 700 nm (1.77 eV) long-pass filters. In all of the presented results, the pump and signal beams have linear polarizations, rotated by a zero-order 405 nm (3.06 eV) half-wave plate and a broadband (1,100-2,000 nm/0.62-1.13 eV) half-wave plate, respectively. To directly compensate for all of the polarization anisotropies of our set-up (for example, the different s and p polarization reflection and transmission from the beam-splitter plates), the polarization-dependent measurements shown in Fig. 2a and Fig. 2b are acquired in two configurations: 0° and 90°. In the first configuration the sample is mounted at 0° (H) with respect to the laboratory frame of reference, and the incoming polarization directions are set. In the second configuration the sample is mounted at 90° (V) and the incoming polarization directions are also rotated by 90° with respect to the ones set in the first configuration. The final measurement is the average of the two configurations. In Fig. 2c the incoming polarization directions are set and fixed at 0°. The sample is rotated by a rotational motor from 0° to 360° in steps of 5°. Every efficiency and polar measurement is taken on the same spot. Beams are aligned on the sample with submicron precision by an imaging system, allowing us to simultaneously visualize the sample and the two laser beams, coupled with a motorized stage on which the sample is mounted. The sample stage can be manipulated both manually (in-plane travel range of 5 cm) and by a Physik Instrumente piezo-motor for nanometric step sizes (travel range of a hundred microns). The fine motor is essential to align the beams on the sample with submicron accuracy, in particular on the 1L region of the AA stack sample with lateral dimension of 3-4 µm. We stress the fact that even if the infrared signal spot is about double in size with respect to the VIS pump spot, the nonlinear emission of the idler beam occurs only in the pump-signal overlapping region, that is ${\sim}1\,\mu m$. Indeed by displacing the 1L area sample with the piezo-motor by submicron steps around the centre, we detect no appreciable change in the nonlinear emission spectrum, as shown in the left panel of Fig. 3c.

Parametric amplification by MX2. Following a previously reported approach5, the linear and nonlinear surface conductivities of MX, are calculated from the tight-binding Hamiltonian of the electronic band structure, which is approximated as a $\mathbf{k} \cdot \mathbf{p}$ Hamiltonian $H_0(\mathbf{k}, \tau, s)$ (see Supplementary Note 8), where \mathbf{k} is the electron wave-vector, and τ and s are the valley and spin indexes, respectively. Coupling with external radiation is introduced through the time-dependent Hamiltonian $H_0[\mathbf{k} + (e/\hbar)\mathbf{A}(t), \tau, s]$, where -e is the electron charge, \hbar is the reduced Planck constant, and A(t) is the vector potential that accounts for the signal, idler and pump fields with carrier angular frequencies $\omega_1(\omega_s)$, $\omega_2(\omega_i)$ and ω_3 (ω_p), respectively. Such a time-dependent Hamiltonian leads to the temporal evolution of the density matrix $\dot{\rho} = -(i/\hbar)[H_0(t), \rho] - (1/\tau)(\rho - \rho_0)$, where a phenomenological relaxation is assumed to bring the system to the relaxed state ρ_0 at a rate τ^{-1} with $\hbar \tau^{-1} = 50$ meV (that is, the relaxation time is taken as $\tau \approx 13$ fs). We solve perturbatively the density matrix equations of MX2 in the weak excitation limit and in the slowly varying envelope approximation (see Supplementary Note 8), obtaining the surface current density

$$J(t) = \operatorname{Re} \left\{ \sum_{j=1}^{3} \left[\sigma_{L}(\omega_{j}) A_{j}(t) \hat{\mathbf{n}}_{j} e^{-i\omega_{j}t} \right] + \right. \\ \left. + \sigma_{2}(\omega_{1}, \omega_{2}) A_{1}(t) A_{2}(t) \mathcal{M}(\hat{\mathbf{n}}_{1}) \hat{\mathbf{n}}_{2} e^{-i\omega_{3}t} + \right. \\ \left. + \sigma_{2}(\omega_{1}, \omega_{3}) A_{1}^{*}(t) A_{3}(t) \mathcal{M}(\hat{\mathbf{n}}_{1}) \hat{\mathbf{n}}_{3} e^{-i\omega_{2}t} + \right. \\ \left. + \sigma_{2}(\omega_{2}, \omega_{3}) A_{2}^{*}(t) A_{3}(t) \mathcal{M}(\hat{\mathbf{n}}_{2}) \hat{\mathbf{n}}_{3} e^{-i\omega_{1}t} \right\},$$

$$(1)$$

where $\sigma_{\rm L}(\omega_j)$ (j=1,2,3) and $\sigma_2(\omega_p,\omega_m)$ (l,m=1,2,3) are the linear and nonlinear mixing conductivities, $\hat{\bf n}_j$ are in-plane linear polarization vectors, $\hat{\bf n}_j = \cos\theta_j\hat{\bf x} + \sin\theta_j\hat{\bf y}$, defined in terms of angles θ_j with respect to the zigzag edge (oriented along $\hat{\bf x}$),

$$\mathcal{M}(\hat{\mathbf{n}}_j) = \begin{pmatrix} \hat{\mathbf{n}}_j \cdot \hat{\mathbf{y}} & \hat{\mathbf{n}}_j \cdot \hat{\mathbf{x}} \\ \hat{\mathbf{n}}_i \cdot \hat{\mathbf{x}} & -\hat{\mathbf{n}}_i \cdot \hat{\mathbf{y}} \end{pmatrix}, \tag{2}$$

 $\hat{\mathbf{x}}$, $\hat{\mathbf{y}}$ are orthogonal unit vectors spanning the MX₂ plane, and $A_j(t)$ are the in-plane signal (j=1), idler (j=2) and pump (j=3) field envelopes. We emphasize that the structure of the matrix $\mathcal{M}(\hat{\mathbf{n}}_j)$ is a direct consequence of the D_{3h} group symmetry of MX₂.

By solving the nonlinear scattering of impinging signal (j=1) and pump (j=3) waves with amplitudes $A_1(t)=A_s(t)$, $A_3(t)=A_p(t)$ and polarization angles $\theta_1=\theta_s$ and $\theta_3=\theta_p$ in the undepleted pump approximation (see Supplementary Note 8), it is possible to calculate analytically the idler field polarization vector

$$\hat{\mathbf{n}}_2 = \cos(\pi/2 - \theta_1 - \theta_3)\hat{\mathbf{x}} + \sin(\pi/2 - \theta_1 - \theta_3)\hat{\mathbf{y}},\tag{3}$$

and the idler envelope

$$A_2(t) = C_1 A_1^*(t) A_3(t) / [C_2 - C_3 |A_3(t)|^2], \tag{4}$$

while we do not report here the cumbersome expressions for the coefficients $\mathcal{C}_1,\mathcal{C}_2,\mathcal{C}_3$ (see Supplementary Note 8). Note that in the weak excitation regime $|A_3(t)|^2 < |\mathcal{C}_2/\mathcal{C}_3|$ the predicted dependence of idler power on pump and signal power is linear $|A_2(t)|^2 \simeq |\mathcal{C}_1/\mathcal{C}_2|^2 |A_1(t)|^2 |A_3(t)|^2$ and the theory well

LETTERS NATURE PHOTONICS

reproduces the experimental findings (see Fig. 1c). The emitted average idler powers reported in Fig. 1 are calculated as $P_i = (1/2)\tau_{\rm rep}^{-1}e_0 c \int_{-\tau_{\rm rep}}^{\tau_{\rm rep}/2} |A_2(t)|^2 dt$, where we have considered the laser repetition period $\tau_{\rm rep} = 12.5$ ns, input signal and pump envelopes $A_j(t) = A_j \exp(-t^2/2\tau^2)$ (j=1,3) with duration $\tau=250$ fs and amplitudes $A_j = \sqrt{2I_j/e_0}c$, where $I_j = 4\log 2P_j\tau/(\pi s_j^2\tau_{\rm rep})$ are peak intensities obtained by averaging over Gaussian spatial profiles with spots $s_1=2\,\mu{\rm m},\,s_3=1\,\mu{\rm m}$ and P_j are the impinging average powers of signal and idler waves. The polarization dependencies illustrated in Figs. 2 and 3 fully reproduce the analytically derived rule $\theta_i=\pi/2-\theta_s-\theta_p$. Finally, the effective bulk $\chi_2(\omega_p,\omega_m)$ responsible for the OPA process can be calculated as

$$\chi_{2}(\omega_{1}, \omega_{2}) = i\sigma_{2}(\omega_{1}, \omega_{2})/(t_{1L}\epsilon_{0}\omega_{3}),
\chi_{2}(\omega_{2}, \omega_{3}) = i\sigma_{2}(\omega_{2}, \omega_{3})/(t_{1L}\epsilon_{0}\omega_{1}),
\chi_{2}(\omega_{1}, \omega_{3}) = i\sigma_{2}(\omega_{1}, \omega_{3})/(t_{1L}\epsilon_{0}\omega_{2}),$$
(5)

where $t_{\rm IL}$ = 0.65 nm is the 1L thickness of MX₂ and ϵ_0 is the dielectric permittivity of vacuum. Our semi-analytical predictions based on independent electron dynamics reproduce well the broadband behaviour of the idler nonlinear generation process but do not account for exciton enhancement, although experimental findings indicate that it plays a minor role in OPA. Future investigations accounting for the role of exciton enhancement will require brute force numerical integration of time-dependent semiconductor Bloch equations 24 .

Data availability

The data that support the plots within this paper and other findings of this study are available from the corresponding author on reasonable request. Source data are provided with this paper.

References

 Liu, F., Ziffer, M. E., Hansen, K. R., Wang, J. & Zhu, X. Direct determination of band-gap renormalization in the photoexcited monolayer MoS₂. *Phys. Rev. Lett.* 122, 246803 (2019).

Acknowledgements

C.T., G.C., P.J.S., J.H. and N.C. acknowledge the project SONAR, which has received funding from the European Union's Horizon 2020 research and innovation programme under the Marie Skłodowska–Curie grant agreement (no. 734690). G.C. acknowledges

support by the European Union Horizon 2020 Programme under grant agreement no. 881603 Graphene Core 3. A.M. acknowledges support from the Rita Levi Montalcini Fellowship (grant no. PGR15PCCQ5) funded by the Italian Ministry of Education, Universities and Research (MIUR). A.C. acknowledges PRIN 2017 PELM (grant no. 20177PSCKT). X.Z. acknowledges support for the Vannevar Bush Faculty Fellowship through ONR grant N00014-18-1-2080 for sample preparation, and partial support by the National Science Foundation (NSF) grant DMR-1809680 for the development of the exfoliation technique. This research was supported in part by the Department of Energy (DOE) Office of Energy Efficiency and Renewable Energy (EERE) Postdoctoral Research Award under the EERE Solar Energy Technologies Office administered by the Oak Ridge Institute for Science and Education (ORISE) for the DOE. ORISE is managed by Oak Ridge Associated Universities (ORAU) under DOE contract no. DE-SC00014664. All opinions expressed in this paper are the author's and do not necessarily reflect the policies and views of DOE, ORAU or ORISE. P.J.S., J.H. and K.Y. acknowledge support from Columbia University's Fu Foundation School of Engineering and Applied Science Interdisciplinary Research Seed (SIRS) Funding program. Portions of this work are supported as part of Programmable Quantum Materials, an Energy Frontier Research Center funded by the US Department of Energy (DOE), Office of Science, Basic Energy Sciences (BES), under award DE-SC0019443.

Author contributions

C.T. designed the experiment, built the set-up, performed the measurements and wrote the manuscript. A.M. performed the theoretical calculations and wrote the manuscript. X.X. and C.L. performed the measurements. F.L. and N.C. prepared the sample. C.M. designed the experiment and performed part of the theoretical calculations. A.C. performed part of the theoretical calculations. S.D.C. helped in the design of the experiment. J.H., X.Z., P.J.S. supervised the experiments and wrote the manuscript. G.C. designed and supervised the experiment, and wrote the manuscript.

Competing interests

The authors declare no competing interest.

Additional information

Supplementary information is available for this paper at https://doi.org/10.1038/s41566-020-00728-0.

Correspondence and requests for materials should be addressed to P.J.S. or G.C.Reprints and permissions information is available at www.nature.com/reprints.